

Use of multi-pollutant air sensor data and geometric non-negative matrix factorization for source apportionment of air pollution burden in Curtis Bay, Baltimore, USA

Bora Jin†, Bonita D. Salmerón‡, David McClosky‡, David H. Hagan‡, Russell R. Dickerson§,
Nicholas J. Spada§, Lauren N. Deanes‡, Matthew A. Aubourg‡, Laura E. Schmidt‡, Gregory G.
Sawtell§, Christopher D. Heaney‡¶#, Abhirup Datta†*

[†]Department of Biostatistics, Johns Hopkins Bloomberg School of Public Health, Baltimore,
MD, 21205, USA

[‡]Community Science and Innovation for Environmental Justice Initiative, Center for a Livable
Future, Department of Environmental Health and Engineering, Johns Hopkins Bloomberg
School of Public Health, Baltimore, MD, 21205, USA

[§]Department of Epidemiology, Johns Hopkins Bloomberg School of Public Health, Baltimore,
MD, 21205, USA

[#]Department of International Health, Johns Hopkins Bloomberg School of Public Health,
Baltimore, MD, 21205, USA

‡QuantAQ, Inc, Somerville, MA, 02143, USA

¥Department of Atmospheric and Oceanic Science, University of Maryland, College Park, MD, 20742, USA

°Air Quality Research Center, University of California, Davis, CA, 95616, USA

§Community of Curtis Bay Association, Baltimore, MD, 21226, USA and South Baltimore Community Land Trust, Baltimore, MD, 21225, USA

ABSTRACT

Air sensor networks provide hyperlocal, high temporal resolution data on multiple pollutants that can support credible identification of common pollution sources. Source apportionment using least squares-based non-negative matrix factorization is non-unique and often does not scale. A recent geometric source apportionment framework focuses inference on the source attribution matrix, which is shown to remain identifiable even when the factorization is not. Recognizing that the method scales with and benefits from large data volumes, we use this geometric method to analyze 451,946 one-minute air sensor records from Curtis Bay (Baltimore, USA), collected from October 21, 2022 to June 16, 2023, covering size-resolved particulate matter (PM), black carbon (BC), carbon monoxide (CO), nitric oxide (NO), and nitrogen dioxide (NO₂). The analysis identifies three stable sources. Source 1 explains > 70% of fine and coarse PM and ~30% of BC. Source 2 dominates CO and contributes ~70% of BC, NO, and NO₂. Source 3 is specific to the larger PM fractions, PM₁₀ to PM₄₀. Regression analyses show Source 1 and Source 3 rise during bulldozer activity at a nearby coal terminal and under winds from the

terminal, indicating a direct coal terminal influence, while Source 2 exhibits diurnal patterns consistent with traffic. A case-study on the day with a known bulldozer incident at the coal terminal further confirms the association of terminal activities with Sources 1 and 3. The results are stable under sensitivity analyses. The analysis demonstrates that geometric source apportionment, paired with high temporal resolution data from multi-pollutant air sensor networks, delivers scalable and reliable evidence to inform mitigation strategies.

KEYWORDS

Air pollution, Baltimore, Big data, Coal terminal, Convex geometry, Source apportionment.

SYNOPSIS

For decades, Curtis Bay community residents have observed and reported the accumulation of dark dust at and in their homes, which many attribute to the operation of a neighboring open-air coal terminal. This research contributes scientific support of community observations, can inform local regulatory decision making, and presents a scalable and reliable application of non-negative matrix factorization as an air pollution source apportionment approach.

Introduction

Air pollutants in communities arise from multiple sources, and policy action depends on knowing which sources dominate each pollutant. Source apportionment analysis addresses this need by quantifying contributions of latent factors or sources to observed concentrations. Source apportionment, also termed multiple receptor modeling, is often posed as a non-negative matrix factorization (NMF) problem and solved by (weighted) least squares^{1,2}. Positive matrix

factorization (PMF)³ is one of the most widely used methods for source apportionment. Generic NMF software (in Python or R) is also commonly used, which also relies on least squares. More specialized extensions accommodate temporal⁴ and spatial⁵ correlation across multi-pollutant data and admit Bayesian formulations^{6,7}. However, NMF is generally non-unique, and the factor matrices are not individually identifiable or interpretable, unless imposing strong assumptions. This challenge is well-known and acknowledged by NMF-based methods, and mitigation strategies often involve promoting sparse solutions, but do not guarantee uniqueness. For example, the Environmental Protection Agency's (EPA) documentation of PMF⁸ explicitly acknowledges this non-identifiability and provides rotation controls such as Fpeak to explore either sparser or more diffuse solutions.

Recent rise in usage of multi-pollutant air sensor networks^{9,10} for exposure assessment presents the opportunity to conduct source apportionment studies at locally-relevant spatio-temporal scales. These sensors offer spatially and temporally dense data which can aid in understanding major sources of pollutants in communities. However, the high temporal resolution (second- or minute-level) data from air sensors leads to large datasets that also pose a scalability challenge to some existing source apportionment tools.

In other scientific applications, unrelated to source apportionment, there is a long history of using geometric ideas for NMF, viewing the data matrix as a point cloud in a conical hull, where the corners become factor profiles after suitable scaling. Geometric NMF has found use in vertex hyperspectral unmixing, often referred to as vertex component analysis or endmember extraction¹¹⁻¹³. Conditions for geometric identifiability of NMF factors in these applications are formalized¹⁴, and many algorithms are available leveraging convex hull geometry. While there is some early work connecting these ideas to source apportionment¹⁵, existing implementations are

not compatible with modern computing environments, and these geometric NMF ideas have been largely underutilized in air pollution source apportionment.

Recent work on geometric NMF¹⁶ has demonstrated how these geometric ideas can lead to provably reliable source apportionment. Instead of trying to infer the individual NMF factors, they consider an identifiable estimand, the source attribution matrix, which is the percentage of concentrations of each pollutant attributable to each source. This matrix is shown to be unique, scale-invariant, and interpretable even when the factors in NMF are not. Under weaker and more realistic assumptions than those typically required for factor identifiability, they provide a geometric algorithm for estimation of this source attribution matrix along with accuracy guarantees of the estimator.

In this manuscript, we apply the geometric NMF¹⁶ for source apportionment in Curtis Bay (Baltimore, USA) using a large multi-pollutant dataset of nearly half-a-million observations from ambient hyperlocal air sensing in the community. This dataset is well matched to geometric NMF. Large sample sizes allow the point cloud to populate the conical hull, improving estimation of source profiles; the high-volume sensor data are therefore a clear advantage. Curtis Bay is a neighborhood with a high density residential population living in proximity to a heavy concentration of industrial facilities and air pollution emissions¹⁷. One facility, an open-air coal export terminal operated by CSX Corporation, has been a longstanding source of community environmental health concerns related to air pollution burden^{17,18} and fugitive dark dust, which has been demonstrated to contain coal dust¹⁹, at homes, businesses, schools, and churches in Curtis Bay. While impacts of coal mining on air quality and health are well documented²⁰, much less is known about the influence of open air coal export terminals. Since source apportionment analysis can identify latent sources and quantify their intensity from pollutant data alone, without

using prior information about nearby facilities, our analysis allows for an unsupervised assessment of whether an air pollution source that is attributable to coal terminal activities emerges among the major pollution sources in Curtis Bay.

Materials and Methods

Data

Data were collected in Curtis Bay through a community-driven collaboration among the Community of Curtis Bay Association (CCBA), the South Baltimore Community Land Trust (SBCLT), academic partners, and the Maryland Department of the Environment (MDE) to evaluate the potential impacts of the coal terminal on Curtis Bay air pollution burden; details of the collaboration are available elsewhere¹⁹.

At four sites (Locations 1, 2, 5, and 8) in Curtis Bay, we deployed QuantAQ MODULAIR monitors (QuantAQ Inc., Somerville, MA) to measure particulate matter (PM) concentrations: PM₁, PM_{2.5}, PM₁₀, total suspended particles (TSP; equivalent to PM₄₀) in $\mu\text{g}/\text{m}^3$; gases: carbon monoxide (CO), nitric oxide (NO), and nitrogen dioxide (NO₂) in ppb; and temperature in degrees Celsius. Each MODULAIR was paired with a sonic anemometer (Davis Instruments Corp., Hayward, CA) to record wind speed in miles per hour and direction in degrees. A binary downwind indicator was constructed for each site relative to the coal terminal based on measured wind direction. We also deployed Distributed Sensing Technologies (DSTech) ObservAir sensors to measure black carbon (BC) in $\mu\text{g}/\text{m}^3$. Trail-camera footage (CamPark Electronics Co., Ltd, Hong Kong) near Location 5 was used to identify coal terminal activities, including visible bulldozer operation, which informed a binary minute-level visible bulldozer activity time-series. All measurements were collected at 1-minute resolution. Hourly solar radiation in W/m^2 from the

MDE's Essex station (~15 km from Curtis Bay) was mapped to the corresponding minute-level observations. We applied previously described data processing and quality assurance/quality control procedures and refer readers to the same source for monitoring locations and the detailed definition of the downwind variable¹⁸.

For source apportionment, we first formed non-overlapping bins in terms of PM size increments: PM_{2.5}-PM₁, PM₁₀-PM_{2.5}, TSP-PM₁₀ to avoid double counting across size bins. We retained complete-case minute-level observations with all of the following measurements available: PM₁, PM_{2.5}-PM₁, PM₁₀-PM_{2.5}, TSP-PM₁₀, BC, CO, NO, and NO₂. We additionally removed two clear outliers in TSP-PM₁₀, yielding a total of 451,946 minute-level records spanning 11:21 am on October 21, 2022, to 11:59 pm on June 16, 2023. Meteorological and coal terminal activity variables may have fewer observations due to missingness, but they are not used in the main source apportionment analysis, only for subsequent regression analysis.

Infrequently (45,039 measurements; < 10% of data), BC has negative values, which has been described in detail previously¹⁸. Because source apportionment relies on non-negative matrix factorization, and thus requires non-negative inputs, we retain negative values but apply an offset transform that preserves ranks. We also apply quantile-based scaling which respects each pollutant's measured range, avoiding the over-compression that occurs when pollutants with heavy tails are normalized to a fixed range (e.g. [0,1]). For pollutant j , let m_j be the minimum and $q_{0.85,j}$ be the 85th percentile. We transform the measured concentration Y_{ij}^0 to $Y_{ij} = \{Y_{ij}^0 - \min(m_j, 0)\}/(q_{0.85,j} - m_j)$. The mean shift is applied only when $m_j < 0$, and the scaling by $q_{0.85,j} - m_j$ provides outlier-robust normalization. We use 85th percentile because all pollutants

are highly skewed. For example, TSP-PM₁₀ is so skewed that its values are essentially zero below this point and become nonzero only beyond it.

Additionally, traffic count and classification data were collected using the Houston Radar Armadillo Tracker (Houston Radar LLC, Sugarland, TX) on Pennington Avenue and Curtis Avenue, two parallel routes in Curtis Bay. For each detected vehicle, the device records time and date of the event and vehicle class (small, medium or large vehicle). Per manufacturer specifications, the accuracy of vehicle counts is up to 97% for the local road configurations for typical free flowing traffic, with potential decreased accuracy for stop and go traffic²¹. Classifications were based on vehicle length with a length of < 4 m counted as small vehicles, between 4 and 7 m as medium vehicle, and > 7 m as large vehicles. Data were collected periodically between February 19, 2025 and November 5, 2025 for a total collection of 134.8 days, or 3,234.2 hours.

A brief review of non-negative matrix factorization and source apportionment methods

Let $Y \in \mathbb{R}^{n \times J}$ denote the (possibly normalized) concentrations for J pollutants at n timepoints. The $(i, j)^{\text{th}}$ entry of Y is the measured concentration of pollutant j at time i . With K sources, the premise of source apportionment is that the data matrix can be represented as a non-negative matrix factorization $Y \approx WH$, where $W = (W_{ik}) \in \mathbb{R}^{n \times K}$ represents source intensity and $H = (H_{kj}) \in \mathbb{R}^{K \times J}$ the per-unit source profiles.

Some source apportionment methods (e.g., chemical mass balance^{22,23}) assume the source profiles to be known, in which case, the problem simply becomes a regression model. Other methods such as PMF and generic NMF treat both W and H to be unknown, and are more in the spirit of factor models. All these methods use some variant of least squares optimization to

estimate the unknown matrices. However, NMF is fundamentally non-identifiable. This non-identifiability includes scale ambiguity, and one can have a continuum of admissible rotations that cannot be resolved from data alone without additional structure. Conditions for uniqueness require strict sparsity assumptions that are rarely guaranteed in practice for ambient mixtures²⁴. This limitation of least squares based matrix factorization is widely known and various mitigation strategies are adopted. PMF addresses rotational ambiguity with the Fpeak parameter that can be tuned to have sparser or more diffuse solution. It also has provision to incorporate prior information through anchored constraints that nudge selected profile rows or time series toward reference values within uncertainty bounds. These tools can help stabilize factors and improve interpretability. Alongside PMF, penalized sparse NMF variants add explicit sparsity in W and/or H to reduce factor overlap, typically via alternating nonnegativity constrained least squares with sparseness penalties²⁵. In practice, we found least squares based NMF highly unstable to data standardization choices, the inclusion or exclusion of a small number of observations, and the specific algorithms used. Furthermore, the current PMF software does not scale well to large datasets that are now common in practice.

Identifiable geometric source apportionment

Recently a geometric source apportionment framework¹⁶ has been proposed which presents multiple arguments to focus statistical inference not on the individual factor matrices, but on a quantity derived from them: the source attribution percentage matrix $\Phi = (\phi_{kj})$, which is defined by

$$\phi_{kj} = \frac{\mu_k H_{kj}}{\sum_{l=1}^K \mu_l H_{lj}}, \quad \mu_k = E(W_{ik}), \quad (1)$$

where ϕ_{kj} is the fraction of pollutant j attributable to source k (columns sum to one) and $\mu_k = E(W_{ik})$ is the expected (statistical average) intensity for source k (over all time-points).

This estimand Φ has two advantages. (i) Scale invariance: the quantity Φ is unchanged by pollutant-specific unit changes. Thus, it is invariant to the scale ambiguity of individual factors, i.e., Φ is unique even when the NMF is not. (ii) Statistical identifiability under realistic conditions: the matrix Φ can be provably accurately estimated using large datasets. This property is robust to spatio-temporal dependence in pollutant concentrations and does not require any strict sparsity; instead, it only requires that each source occasionally (in a probabilistic sense) dominates the mixture. This probabilistic relaxation is more plausible than deterministic separability or sparsity assumed in other geometric NMF approaches, which unrealistically demands complete absence of other sources.

The source attribution fractions ϕ_{kj} defined in (1) is very similar in spirit to the ‘percent of species’ produced by PMF and reported in other studies⁹: $\sum_i W_{ik} H_{kj} / \sum_i Y_{ij}$. However, they differ in interpretation. We interpret ϕ_{kj} as the share of pollutant j attributable to source k among the K sources; for each pollutant these shares sum to one. In contrast, PMF ‘percent of species’ values for a given pollutant need not add to 100% and can even be more than 100% which is problematic to interpret.

The geometric NMF algorithm we adopt is based on viewing each record of the data matrix Y as a point in a conical hull, or equivalently, each row of the row-normalized data Y^* as a point in a convex hull. More data points allow a better understanding of the shape of the point cloud, leading to a more accurate estimate of the corners of the hull, which are simply the rows of H^* , the row-normalized version of H . Given a specified number of factors K , the algorithm proceeds

by estimating the convex hull, followed by choosing the K -point subset of the hull corners (extreme points) that maximizes the volume of the K -vertex polytope. These points form the rows of estimate of H^* . Subsequently, \tilde{W} (scaled version of W) can be estimated using a constraint linear solve $Y \approx \tilde{W}H^*$, and Φ can be calculated as in (1) using the estimated factor matrices. For technical details, see their Algorithm 1¹⁶.

We tailor the algorithm to handle very large datasets, such as minute-level measurements from multi-pollutant air sensors. For finding the maximum-volume K -subset of extreme points on the sample convex hull with N corners, an exhaustive search over all N -choose- K possibilities is computationally prohibitive. We therefore prune the N hull vertices to retain a well-separated N_0 candidates ($N_0 \ll N$) through k-means clustering, then select K representatives from those N_0 candidates that maximize the polytope volume. Balancing accuracy and cost, we set the pruned vertex set to have $N_0 = 40 \times K$, based on pilot experiments.

Uncertainty quantification and choice of the number of factors

We quantify uncertainty in Φ by repeating the estimation over 100 bootstrap resamples of the data. We select the number of factors K based on estimation stability. Specifically, we summarize (i) the mean cellwise coefficient of variation of the source attributions ϕ_{kj} , computed as the bootstrap standard error (SE) divided by the bootstrap mean and averaged across cells after excluding those with bootstrap mean less than 0.03 to avoid numerical blow-ups; lower is better, and (ii) rank stability of the dominant source, defined for each pollutant as the bootstrap probability that the top source (identified from the bootstrap mean) is preserved, averaged across pollutants; higher is better.

Sensitivity analysis

To assess robustness of our results, we compare them with an alternative geometric method, XRAY²⁶, which also targets convex hull vertices but uses a different strategy to select the K -subset. XRAY iteratively chooses the point that pushes the hull boundary outward the most. We examine results for $K \in \{3,4\}$. We also report least squares NMF results obtained using the widely used Python package scikit-learn and compare how the estimated attribution matrix Φ changes under the default (no regularization) setting versus an L2-penalized fit ($\text{alpha_W} = \text{alpha_H} = 0.001$). We also attempted to use ESAT²⁷, a recently developed Python implementation of PMF5, but it was unable to handle the full data volume on a 2021 MacBook Pro with Apple M1 Pro and 16 GB RAM and we found it challenging to achieve model convergence even on a smaller subset of the data.

Diurnal pattern comparisons

After estimating source intensities, we compare the diurnal averages of each estimated source, the pollutants most strongly attributed to it, and regional traffic counts in Curtis Bay to aid interpretation. Although the time periods of the multi-pollutant and traffic datasets do not align, we expect the diurnal traffic pattern in the area to be stable over time. Given the proximity of the multi-pollutant air sensor locations and the traffic counters, the traffic data should reliably represent general diurnal trends in the study region.

Regression analysis

Subsequent to estimation of the source intensity, to interpret the learned sources, we regress each column of the estimated source intensity matrix \tilde{W} on indicators for bulldozer activity at the coal

terminal (“Bulldozer=1”), being downwind of the terminal (“Downwind=1”), and their interaction, adjusting for NO, temperature, wind speed, time of day (AM/PM), solar radiation, and location (Location 1/2/5/8). We focus on the coefficients for “Bulldozer=1”, “Downwind=1”, and their main effect plus interaction. Because our inference compares intensity within each source rather than across sources, this analysis is robust to column-wise scale ambiguity in W . To validate the source-level coefficients, we fit the same regression models to each pollutant and assess concordance in the estimated direction of the regression coefficients for pollutants and those of the estimated sources. For gas models, NO is excluded as a covariate. We repeat this for each bootstrap replicate to obtain uncertainty estimates of the regression coefficients.

Case study

We present a case study examining the behavior of the estimated source intensity during a reported coal terminal incident involving a bulldozer immobilized on a coal pile on February 3, 2023, from 11:30 am to 2:45 pm local time. To formally compare the incident versus control periods (same hours of the previous and next days), we use one-sided two-sample tests: the Mann-Whitney U (MW) test and the Kolmogorov-Smirnov (KS) test. For the MW test, the null hypothesis is that the incident and control distributions are identical, and the alternative is that the incident distribution is stochastically larger than the control distribution. For the KS test, the null is that the incident distribution is stochastically smaller than or equal to the control distribution, and the alternative is that this null does not hold. Both tests are nonparametric and accommodate unequal sample sizes. P-values are reported from both tests for individual pollutant concentrations.

Results

Summary statistics (count, mean, standard deviation, median, minimum, maximum, 15th, and 85th percentiles) of air pollutants (PMs, BC, and gases) in Curtis Bay are reported in Table 1. We see that the maximum values of certain pollutants are orders of magnitude higher than even their 85th quantiles. For example, the maximum measured concentration of TSP-PM₁₀ (17503.5 $\mu\text{g}/\text{m}^3$) is over 1000 times larger than the 85th percentile (14.2 $\mu\text{g}/\text{m}^3$). Similar phenomenon, albeit to a lesser extent, occurs with most of the other pollutants. Because of such extreme skewness, it is not advisable to scale the data using the maximum values, which leads to squishing most of the information, and we scale using the 85th percentile.

Table 1. Summary statistics of pollutants measured at 1-minute time interval in Curtis Bay.

	Count	Mean (Std)	Min	15th percentile	Median	85th percentile	Max
PM ₁ ($\mu\text{g}/\text{m}^3$)	451946	8.4 (6.3)	0.09	3.2	7.0	13.7	417.0
PM _{2.5} – PM ₁ ($\mu\text{g}/\text{m}^3$)	451946	0.9 (1.4)	0	0.2	0.6	1.6	119.7
PM ₁₀ – PM _{2.5} ($\mu\text{g}/\text{m}^3$)	451946	14.9 (36.6)	0	0.8	6.5	26.1	5233.7
TSP – PM ₁₀ ($\mu\text{g}/\text{m}^3$)	451946	10.7 (148.8)	0	0	0	14.2	17503.5
BC ($\mu\text{g}/\text{m}^3$)	451946	0.8 (1.3)	-10.71	0.1	0.6	1.5	111.8
CO (ppb)	451946	277.7 (178.7)	0.05	179.9	231.1	373.3	11313.5
NO (ppb)	451946	8.2 (15.4)	<0.001	1.7	3.2	11.9	320.4
NO ₂ (ppb)	451946	13.6 (9.1)	<0.001	5.0	11.1	24.5	99.3

A scatter-plot matrix with Pearson correlations and marginal densities appears in Figure 1. The skewness is evident from the marginal densities. The strongest correlation is observed between

PM_{2.5}-PM₁ and PM₁₀-PM_{2.5} (0.7). Moderate correlations (0.3 – 0.5) occurs between several pairs of pollutants, e.g., all pairs of gas pollutants; PM₁ and gases; and BC and gases.

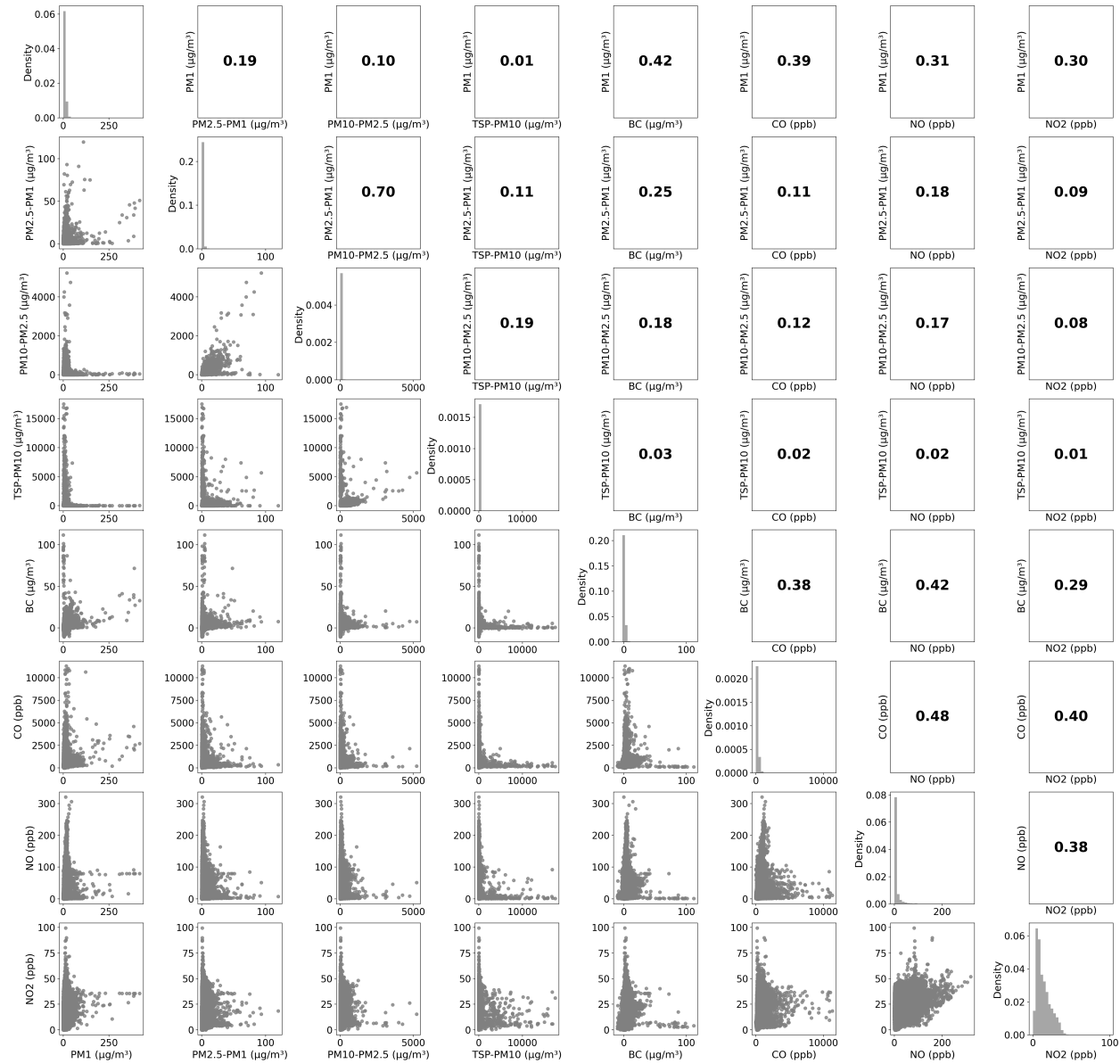


Figure 1. Matrix of air pollutant relationships for Curtis Bay: lower triangle shows pairwise scatter plots, the diagonal displays each pollutant's density, and the upper triangle reports Pearson correlation coefficients. *Note.* PM = particulate matter; TSP = total suspended particles; BC = black carbon; CO = carbon monoxide; NO = nitric oxide; NO₂ = nitrogen dioxide.

Figure 2 presents the main source apportionment results with $K = 3$, reporting the mean estimates and bootstrapped SEs of the source attribution matrix Φ (exact values are reported in Table S1 of the Supporting Information). Source 1 accounts for most of $\text{PM}_{2.5}$ - PM_1 ; and around 70% of each of PM_1 and PM_{10} - $\text{PM}_{2.5}$. Source 1 also contributes ~30% of BC on average, suggesting BC co-occurs with fine to coarse PMs. Source 3 is specific to TSP- PM_{10} , explaining nearly all TSP- PM_{10} , with negligible contributions to all other pollutants. This is consistent with Figure 1 where TSP- PM_{10} shows weak correlations with most other pollutants and indicates a split between larger (TSP- PM_{10}) and fine and coarse (PM_1 ; $\text{PM}_{2.5}$ - PM_1 ; and PM_{10} - $\text{PM}_{2.5}$) PMs. Source 2 is the primary driver of CO and contributes ~70% of each of BC, NO, and NO_2 , with ~25% of PM_1 and PM_{10} - $\text{PM}_{2.5}$. Uncertainty is largest for source contributions for PM_{10} - $\text{PM}_{2.5}$, with Sources 1 and 2 competing to attribute its concentrations.

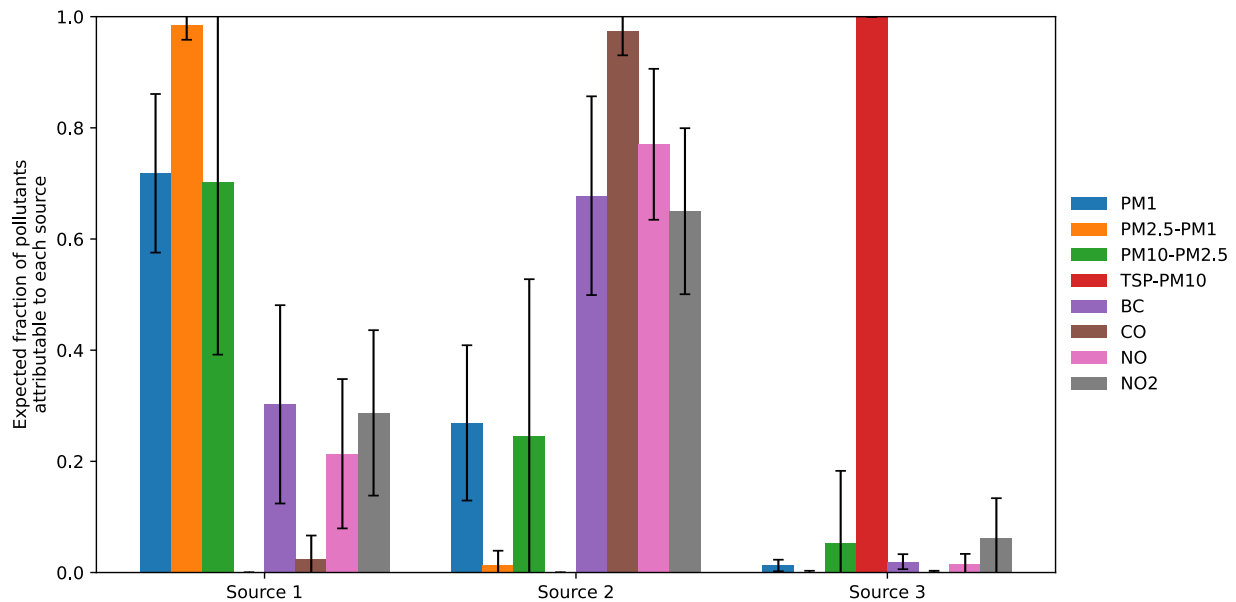


Figure 2. Bootstrap mean \pm standard error of source attributions from the geometric source apportionment method ($K = 3$) across 100 resamples. Bar height denotes the expected fraction of each air pollutant attributable to each source. For a given air pollutant (color), attributions

across sources sum to 1. *Note.* PM = particulate matter; TSP = total suspended particles; BC = black carbon; CO = carbon monoxide; NO = nitric oxide; NO₂ = nitrogen dioxide.

Based on our sensitivity analysis, estimates of Φ are robust under XRAY using the same number of factors K (Figure S1 in Supporting Information). We choose $K = 3$ because (i) it yields a more coherent interpretation than $K = 4$, which primarily partitions existing sources, and (ii) it exhibits greater stability by rank stability (Table S2, Supporting Information). Although coefficients of variation favor $K = 4$, we prioritize rank stability because reliable identification of leading sources has clearer policy implications. We also found that least squares NMF yields broadly similar patterns but with important discrepancies, especially for PM components and BC (Figure S2, Supporting Information). Moreover, the estimates change depending on whether an L2 penalty is used, with differences far exceeding bootstrap uncertainty. This sensitivity undermines the practical reliability of least squares NMF, since in applications we typically do not know whether regularization is appropriate or how strongly it should be applied.

Figure 3 presents the regression analysis results using the estimated source intensity. The top panel reports bootstrap means and 95% confidence intervals (CIs) for the coefficients corresponding to Bulldozer=1, Downwind=1, and these main effects plus the interaction (“Bulldozer=1 \times Downwind=1”). Source 1 is positively associated with both Bulldozer=1 and Downwind=1, indicating a direct coal-terminal influence. Source 3 is largely insensitive to the main effects but increases when bulldozer activity and downwind conditions coincide, suggesting an episodic contribution linked to terminal operations. Source 2 decreases when winds blow from the terminal, suggesting it is not terminal-related; instead, it exhibits clear weekday versus weekend contrasts in intensity magnitude and a pronounced weekday morning peak ($\sim 7 - 8$ am; bottom panel, Figure 3), consistent with traffic-related emissions. This pattern

mirrors the diurnal profiles of traffic-related primary pollutants that Source 2 dominates (CO and NO₂²⁸; Figure S3, Supporting Information). Independent traffic counts likewise confirm the weekday morning peak (Figure S4 in Supporting Information). The traffic record also shows an additional afternoon/evening peak which is not evident in Source 2, likely muted by planetary boundary layer dynamics that flatten late-day peaks²⁹. Similar coefficient patterns appear in regressions on individual pollutants for the corresponding sources (Figure S5 in Supporting Information), akin to the previously documented results¹⁸. Except for CO, most pollutants increase when bulldozer and downwind coincide, supporting the premise that the coal terminal activity is highly associated with elevated concentrations of these pollutants in Curtis Bay.

Figure 4 presents a case study of an incident when a bulldozer was reported to be immobilized on a coal pile at the coal terminal on February 3, 2023 (11:30 am to 2:45 pm local time). To control for diurnal and operational patterns, we compare these incident hours with the same clock hours on the preceding day (February 2) and the following day (February 4). In the figure, incident hours are shown in red and matched hours on the adjacent days are shown in black.

The top panel displays boxplots of bootstrap distributions of intensity percentiles across 100 resamples, with lines connecting bootstrap means. Source 1 shows a clear and substantial elevation beginning near the 70th percentile that becomes more pronounced at higher percentiles, whereas Source 3 exhibits heavier upper tails (prominent after 95th percentile) during the incident with greater high-end variability. Source 2, while elevated during incident, has more uncertainty and does not display a statistically significant change in tail behavior. These findings echo Figure 3, where Sources 1 and 3 respond to the terminal incident while Source 2 does not.

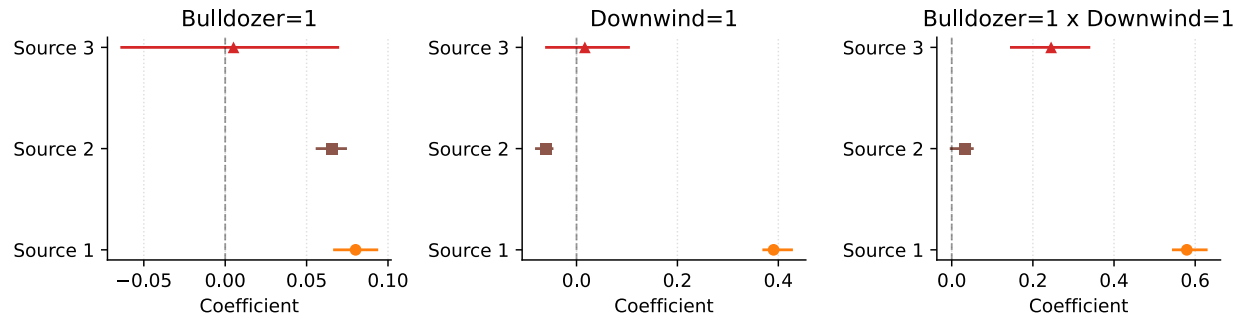


Figure 3. Top: Linear regressions on estimated source intensity. Points and error bar show bootstrap coefficient means with 95% confidence intervals. Bottom: Diurnal averages of estimated intensity from Source 2, shown separately for weekdays and weekends. *Note.* Bulldozer=1 means time period when there was visible bulldozer activity at the coal terminal. Downwind=1 means time period when the direction of the wind was downwind of the coal terminal.

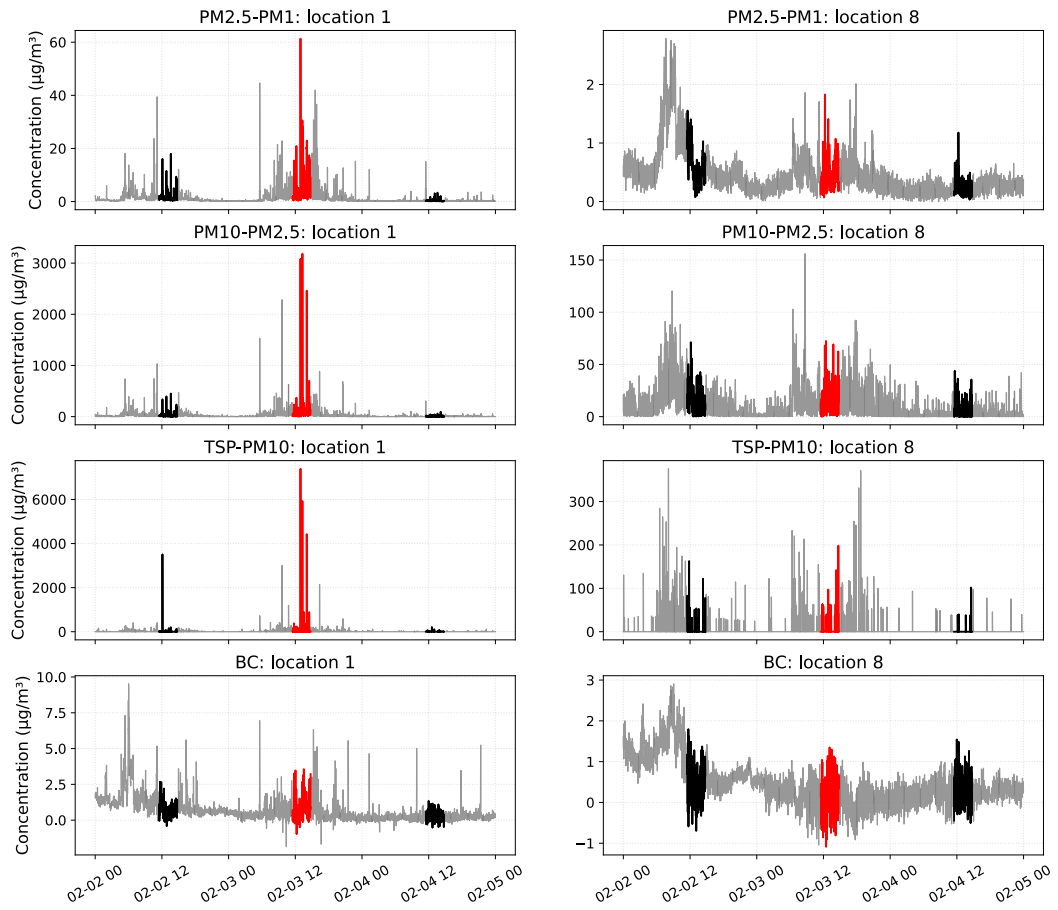
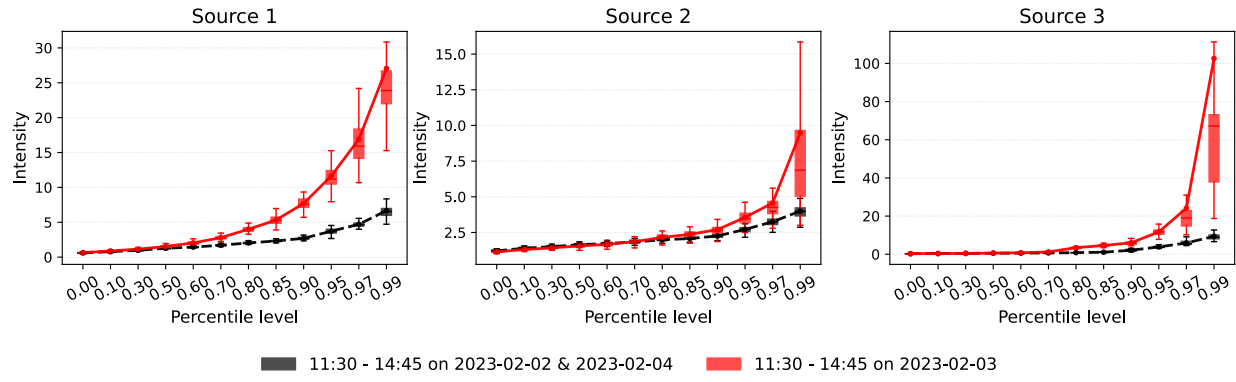


Figure 4. Comparison of air pollution levels during the coal-terminal incident (highlighted in red) versus matched hours (highlighted in black) on other days. Top: percentiles of estimated source intensity across 100 bootstrap resamples; lines connect bootstrap means. Bottom:

location-specific time series of raw concentrations for $\text{PM}_{2.5}$ - PM_1 , PM_{10} - $\text{PM}_{2.5}$, TSP - PM_{10} , and BC . *Note.* PM = particulate matter; TSP = total suspended particles; BC = black carbon.

The bottom panel of Figure 4 shows location-specific time series of raw concentrations for $\text{PM}_{2.5}$ - PM_1 , PM_{10} - $\text{PM}_{2.5}$, TSP - PM_{10} , and BC at the two monitoring sites that recorded data during this window (Locations 1 and 8). At Location 1, which is 0.33 km from the centroid of the terminal, we observe pronounced spikes during the incident relative to the matched hours on other days, while at Location 8, which is 1.22 km away, the effects are attenuated. To formally compare the incident and matched-hour distributions, we use MW and KS tests. At Location 1, $\text{PM}_{2.5}$ - PM_1 , PM_{10} - $\text{PM}_{2.5}$, TSP - PM_{10} , and BC reject the null hypotheses in both tests with p -values ≤ 0.005 suggesting increased concentrations during the incident. At Location 8 only $\text{PM}_{2.5}$ - PM_1 remains significant at the same threshold. This spatial contrast is consistent with proximity-dependent impacts, as finer particles can travel farther from the terminal while coarser fractions are less likely to reach greater distances. Other pollutants do not reject the null in either test even at the significance level of 0.01, whether using pooled data from Locations 1 and 8 or location-specific data, and their time series are shown in Figure S6 of the Supporting Information. Using pooled data from Locations 1 and 8, only $\text{PM}_{2.5}$ - PM_1 , PM_{10} - $\text{PM}_{2.5}$, and TSP - PM_{10} reject the null in both tests at p -value < 0.001 (Table S3, Supporting Information), reflecting elevated contributions from Sources 1 and 3. Taken together, these results suggest that mechanically generated dust and combustion-related aerosol dominated during the incident.

We assessed model adequacy via geometric diagnostics and assumption checks. Pairwise scatter plots in Figure S7 (Supporting Information) show that the estimated source profiles closely align with the vertices of the sample hull. We also examined the probabilistic separability condition underlying the method, which requires that for each source $k \in \{1,2,3\}$, the row-normalized

source intensity W_{ik}^* places non-negligible probability mass near one. The empirical distributions of W_{ik}^* are consistent with this requirement (Figure S8, Supporting Information). On a 2021 MacBook Pro with Apple M1 Pro and 16 GB RAM, using Python 3.11, each bootstrap run with three sources took 10 minutes on average.

Table 2. Summary statistics for air pollutants of interest by locations during the coal-terminal incident versus matched hours on the preceding and following days. We also report p-values from the MW and KS tests.

<i>Location 1</i>	Incident	Count	Mean (Std)	Median	85 th percentile	95 th percentile	Max	p-value (MW)	p-value (KS)
PM _{2.5} – PM ₁ ($\mu\text{g}/\text{m}^3$)	1	196	4.6 (6.5)	2.4	8.3	15.4	61.3	<0.001	<0.001
	0	392	1.0 (1.6)	0.5	1.5	2.7	18.0		
PM ₁₀ – PM _{2.5} ($\mu\text{g}/\text{m}^3$)	1	196	121.2 (364.0)	47.3	145.9	264.2	3184.5	<0.001	<0.001
	0	392	19.2 (42.3)	7.3	30.6	59.0	451.2		
TSP – PM ₁₀ ($\mu\text{g}/\text{m}^3$)	1	196	134.2 (747.7)	0	82.5	246.7	7392.3	<0.001	<0.001
	0	392	15.4 (178.5)	0	0	43.0	3509.3		
BC ($\mu\text{g}/\text{m}^3$)	1	196	0.8 (0.8)	0.6	1.5	2.3	3.6	0.005	0.001
	0	392	0.6 (0.5)	0.5	1.1	1.5	2.7		

<i>Location 8</i>	Incident	Count	Mean (Std)	Median	85 th percentile	95 th percentile	Max	p-value (MW)	p-value (KS)
PM _{2.5} – PM ₁ ($\mu\text{g}/\text{m}^3$)	1	196	0.5 (0.2)	0.4	0.7	0.9	1.8	<0.001	<0.001
	0	392	0.4 (0.3)	0.4	0.8	1.1	1.6		
PM ₁₀ – PM _{2.5} ($\mu\text{g}/\text{m}^3$)	1	196	14.9 (14.7)	9.7	30.7	41.0	72.5	0.029	0.003
	0	392	8.8 (11.5)	3.9	20.8	32.3	71.3		
TSP – PM ₁₀ ($\mu\text{g}/\text{m}^3$)	1	196	7.1 (23.8)	0	0	59.5	198.4	0.046	0.260
	0	392	3.9 (16.3)	0	0	31.7	162.9		
BC ($\mu\text{g}/\text{m}^3$)	1	196	0.2 (0.5)	0.1	0.6	0.9	1.3	1	1
	0	392	0.5 (0.4)	0.5	0.9	1.1	1.8		

Discussion

This study provides the first, to the best of our knowledge, application of a scalable, reliable geometric NMF approach to source apportionment of hyper-local, high temporal resolution multi-pollutant air sensor data. The geometric NMF yields the identifiable source attribution matrix, which we leverage to address longstanding community-raised concerns with specific sources in community air pollution burden. This approach allowed investigation of hypotheses related to specific industrial facilities, events, and activities of concern to local community members that have been complex and difficult to disentangle within the context of cumulative impacts and local air pollution burdens.

The geometric NMF analysis revealed strong evidence of sources related to traffic and the coal terminal in Curtis Bay without relying on any prior information about local industry. The terminal-related findings align with those of previous work on the association of individual air pollutants with a downwind direction of and visible bulldozer activities at the Curtis Bay coal terminal¹⁸. That study observed enhancements in PM across fine, coarse, and larger TSP size ranges as well as BC during times of downwind and bulldozer activity, with consistent evidence of joint effects when both occurred simultaneously. Our analysis recovered Source 1 (contributing to fine to coarse PMs and BC) and Source 3 (TSP), demonstrating consistency with enhancements during periods of downwind and bulldozer activity. On a day when a bulldozer was immobilized on a coal pile at the terminal, the estimated intensity of Sources 1 and 3 showed marked and statistically significant elevations compared to the same time periods on the previous and subsequent days, with the differences being more prominent at the air sensor location closest

to the coal terminal. Source 2, which contributes to CO, NO, NO₂, BC, and to a lesser extent, PM₁, aligns most closely with traffic related air pollutant emissions in Curtis Bay.

The identification of Source 1 as a major contributor to PMs of varying size fraction and BC has important implications for health. Exposure to fine PMs (PM₁ and PM_{2.5}) is a significant health concern due to their ability to penetrate deep into the respiratory tract and bloodstream, which can exacerbate cardiovascular and respiratory conditions. Acute exposure to PM₁₀ has been found to be associated with increased hospital admissions for asthma, bronchitis, and chronic obstructive pulmonary disease and heightened risks of stroke and cardiac events^{30,31}. Acute and long-term exposure to BC has been linked to morbidity and mortality due to cardiovascular and respiratory disease^{32,33}, as well as impacts on fetal, pediatric, and maternal health outcomes³⁴. The risk of adverse health outcomes posed by exposure to each of these pollutants individually has the potential to be compounded when they co-occur in the context of a common source of exposure.

Overall, the geometric NMF approach provides a practical, reproducible framework to understand complex dynamics and patterns of co-occurring air pollutants in a community experiencing the cumulative impacts of diesel combustion and traffic as well as ~70+ industrial facilities with air pollutant emission permits overseen by MDE. Our analysis demonstrates how this approach can help fenceline communities begin to quantify and separate drivers of air pollution burden and advance evidence-based policy solutions to reduce exposure and improve health.

This study has two main strengths. First, the geometric source apportionment framework promotes identifiability and practicality. Least squares NMF centered on source profiles may be

unreliable due to scale ambiguity, which limits interpretability. Moreover, historically popular methods such as PMF often do not scale to large datasets and offer little guidance on penalty terms to enforce uniqueness. In contrast, the geometric approach we adopted in this study focuses inference on the source attribution matrix, which remains uniquely identifiable even when the factorization is not. The geometric NMF requires no penalty-term tuning, eliminating ad hoc regularization choices. The geometric method demonstrated its practical applicability by analyzing high dimensional data with nearly half a million records on a standard laptop, without the need for a high-performance computing cluster. Second, as a community-driven research output, community members from Curtis Bay and South Baltimore, through the CCBA and the SBCLT, guided the research questions investigated, supported deployment of multi-pollutant air sensors, and contributed to the interpretation of the data analysis and its outputs. This included the evaluation of the coherence of the present study's findings with those of prior studies that confirmed the presence of coal dust within settled dark dust collected in Curtis Bay¹⁹ and that demonstrated increased PM and BC air pollution burden related to the coal terminal in Curtis Bay¹⁸. The participatory approach of these studies improves the relevance of the scientific findings to answer longstanding community questions about complex exposure and health burdens related to community-identified sources of concern as well as to inform policy and regulatory decision-making that can mitigate source-specific and cumulative burdens of air pollution exposure.

This study has several limitations. We excluded about 90% of time records because the current geometric NMF method requires complete data. Going forward, a Bayesian version that can fill in missing values, choose the number of sources automatically, and carry uncertainty through to health and policy metrics would be valuable. The present approach also assumes noise-free

measurements, which is rarely true; adding robustness to measurement error and non-stationarity would better suit large spatio-temporal air quality datasets. Regarding downstream analysis, we investigated associations with downwind direction and bulldozer activity at 1-minute time resolution, without investigating potential time-lag effects. Future studies could investigate longer time scales within the context of community lived experiences with the acute / transient nature of mechanically generated, wind-blown dusts (perhaps examining time scales up to 60 minute averages) and examine whether exposure-response associations are enhanced at time lags informed by fate, transport, and dispersion dynamics of varying particle size distributions. Future studies are warranted to elucidate the health impacts of the quantitative outputs of geometric NMF. Such studies could integrate source intensity (reflecting mixtures of co-occurring air pollutants) as exposure variables in longitudinal, repeated-measures epidemiologic studies that focus on biologically relevant health effects, including respiratory, cardiovascular, and health-related quality of life outcomes.

ASSOCIATED CONTENT

Supporting Information: Additional sensitivity analysis details and complementary figures and tables supporting the manuscript's main results (PDF).

AUTHOR INFORMATION

Corresponding Author

[*bjin9@jh.edu](mailto:bjin9@jh.edu)

Funding Sources

This work is partially supported by National Institute of Environmental Health Sciences (NIEHS) grant R01ES033739 and NIEHS P30 Center for Community Health: Addressing Regional Maryland Environmental Determinants of Disease (CHARMED) [grant no. P30ES032756]. BDS, MAA, LES, and CDH were supported by the Johns Hopkins Community Science and Innovation for Environmental Justice (CSI EJ) Initiative. MAA and CDH were supported by NIEHS grant no. P30ES032756. CDH was supported by the National Institute for Occupational Safety and Health (NIOSH) Education and Research Center [grant no. T42OH0008428]. LND was supported by NIEHS Training Program in Environmental Health Sciences [grant no. T32ES007141]. NJS was supported by the UC Davis Environmental Health Science Center Core [grant no. P30ES023513]. RRD was supported by the University of Maryland Challenge Grant and the Maryland Department of the Environment. RRD and the CCBA were supported by the EPA American Rescue Plan Enhanced Air Quality Monitoring for Communities (EPA-OAR-OAQPS-22-01) [grant no. U00P4600952].

ACKNOWLEDGMENT

We thank the Curtis Bay residents, local business owners, and faith-based organizations who trusted our team, contributed their lived experiences and knowledge, and hosted air quality monitors and/or trail cameras. We thank Carlos C. Sanchez-Gonzales, David Jones, and Angela Shaneyfelt for their contributions to and support of this work. We thank the students in the environmental justice class at Benjamin Franklin High School for their engagement and enthusiasm. We thank the Maryland Department of the Environment Air and Radiation Administration for their technical support and collaboration. We thank Anna Hodshire and Eben Cross from QuantAQ and Troy Cados, Julien Caubel, and Nick Wong from Distributed Sensing Technologies for their scientific guidance and technical support.

CONFLICTS OF INTEREST

MAA serves as an unpaid member of the board of directors of the SBCLT, starting on June 24, 2024. The other authors declare that they have no known competing financial interests or personal relationships that could have appeared to influence the work reported in this paper.

References

- (1) Krall, J. R.; Chang, H. H. Statistical Methods for Source Apportionment. In *Handbook of Environmental and Ecological Statistics*; Chapman and Hall/CRC, 2019.
- (2) Hopke, P. K. Review of Receptor Modeling Methods for Source Apportionment. *J. Air Waste Manag. Assoc.* **2016**, *66* (3), 237–259.
<https://doi.org/10.1080/10962247.2016.1140693>.
- (3) Paatero, P.; Tapper, U. Positive Matrix Factorization: A Non-Negative Factor Model with Optimal Utilization of Error Estimates of Data Values. *Environmetrics* **1994**, *5* (2), 111–126.
<https://doi.org/10.1002/env.3170050203>.
- (4) Park, E. S.; Guttorp, P.; Henry, R. C. Multivariate Receptor Modeling for Temporally Correlated Data by Using MCMC. *J. Am. Stat. Assoc.* **2001**, *96* (456), 1171–1183.
<https://doi.org/10.1198/016214501753381823>.
- (5) Jun, M.; Park, E. S. Multivariate Receptor Models for Spatially Correlated Multipollutant Data. *Technometrics* **2013**, *55* (3), 309–320. <https://doi.org/10.1080/00401706.2013.765321>.
- (6) Park, E. S.; Oh, M.-S. Robust Bayesian Multivariate Receptor Modeling. *Chemom. Intell. Lab. Syst.* **2015**, *149*, 215–226. <https://doi.org/10.1016/j.chemolab.2015.08.021>.
- (7) Dai, T.; Dai, Q.; Yin, J.; Chen, J.; Liu, B.; Bi, X.; Wu, J.; Zhang, Y.; Feng, Y. Spatial Source Apportionment of Airborne Coarse Particulate Matter Using PMF-Bayesian Receptor Model. *Sci. Total Environ.* **2024**, *917*, 170235.
<https://doi.org/10.1016/j.scitotenv.2024.170235>.
- (8) US EPA. *EPA Positive Matrix Factorization 5.0 fundamentals and user guide*. <https://www.epa.gov/air-research/epa-positive-matrix-factorization-50-fundamentals-and-user-guide> (accessed 2025-09-17).
- (9) Hagan, D. H.; Gani, S.; Bhandari, S.; Patel, K.; Habib, G.; Apte, J. S.; Hildebrandt Ruiz, L.; Kroll, J. H. Inferring Aerosol Sources from Low-Cost Air Quality Sensor Measurements: A Case Study in Delhi, India. *Environ. Sci. Technol. Lett.* **2019**, *6* (8), 467–472.
<https://doi.org/10.1021/acs.estlett.9b00393>.
- (10) Thorson, J.; Collier-Oxandale, A.; Hannigan, M. Using a Low-Cost Sensor Array and Machine Learning Techniques to Detect Complex Pollutant Mixtures and Identify Likely Sources. *Sensors* **2019**, *19* (17), 3723. <https://doi.org/10.3390/s19173723>.
- (11) Winter, M. E. N-FINDR: An Algorithm for Fast Autonomous Spectral End-Member Determination in Hyperspectral Data. In *Imaging Spectrometry V*; SPIE, 1999; Vol. 3753, pp 266–275. <https://doi.org/10.1117/12.366289>.
- (12) Araújo, M. C. U.; Saldanha, T. C. B.; Galvão, R. K. H.; Yoneyama, T.; Chame, H. C.; Visani, V. The Successive Projections Algorithm for Variable Selection in Spectroscopic

Multicomponent Analysis. *Chemom. Intell. Lab. Syst.* **2001**, *57* (2), 65–73. [https://doi.org/10.1016/S0169-7439\(01\)00119-8](https://doi.org/10.1016/S0169-7439(01)00119-8).

(13) Nascimento, J. M. P.; Dias, J. M. B. Vertex Component Analysis: A Fast Algorithm to Unmix Hyperspectral Data. *IEEE Trans. Geosci. Remote Sens.* **2005**, *43* (4), 898–910. <https://doi.org/10.1109/TGRS.2005.844293>.

(14) Donoho, D.; Stodden, V. When Does Non-Negative Matrix Factorization Give a Correct Decomposition into Parts? In *Advances in Neural Information Processing Systems*; MIT Press, 2003; Vol. 16.

(15) Henry, R. C. Multivariate Receptor Modeling by *N*-Dimensional Edge Detection. *Chemom. Intell. Lab. Syst.* **2003**, *65* (2), 179–189. [https://doi.org/10.1016/S0169-7439\(02\)00108-9](https://doi.org/10.1016/S0169-7439(02)00108-9).

(16) Jin, B.; Datta, A. Identification in Source Apportionment Using Geometry. arXiv 2025. <https://doi.org/10.48550/arXiv.2510.03616>.

(17) Aubourg, M. A.; Sawtell, G.; Deanes, L.; Fabricant, N.; Thomas, M.; Spicer, K.; Wagar, C.; Campbell, S.; Ulman, A.; Heaney, C. D. Community-Driven Research and Capacity Building to Address Environmental Justice Concerns with Industrial Air Pollution in Curtis Bay, South Baltimore. *Front. Epidemiol.* **2023**, *3*. <https://doi.org/10.3389/fepid.2023.1198321>.

(18) Deanes, L. N.; Salmerón, B. D.; Aubourg, M. A.; Schmidt, L. E.; Spicer, K.; Wagar, C.; Sawtell, G. G.; Sanchez-Gonzalez, C. C.; Jones, D.; Shaneyfelt, A.; Hagan, D. H.; McClosky, D.; Spada, N. J.; Dickerson, R. R.; Ravichandran, V.; Wilson, S. M.; Burman, A.; Datta, A.; Heaney, C. D. Relation of Wind Direction and Coal Terminal Activity Patterns with Air Pollution Burden in a Community Bordering a Coal Export Terminal, Curtis Bay, Maryland, USA. *Air Qual. Atmosphere Health* **2025**, *18* (9), 2805–2821. <https://doi.org/10.1007/s11869-025-01773-w>.

(19) Aubourg, M. A.; Livi, K. J. T.; Sawtell, G. G.; Sanchez-Gonzalez, C. C.; Spada, N. J.; Dickerson, R. R.; Chiou, W.-A.; Kamanzi, C.; Ramachandran, G.; Rule, A. M.; Heaney, C. D. Use of Electron Microscopy to Determine Presence of Coal Dust in a Neighborhood Bordering an Open-Air Coal Terminal in Curtis Bay, Baltimore, Maryland, USA. *Sci. Total Environ.* **2024**, *957*, 176842. <https://doi.org/10.1016/j.scitotenv.2024.176842>.

(20) Chu, Y.; Holladay, J. S.; Qiu, Y.; Tian, X.-L.; Zhou, M. Air Pollution and Mortality Impacts of Coal Mining: Evidence from Coalmine Accidents in China. *J. Environ. Econ. Manag.* **2023**, *121*, 102846. <https://doi.org/10.1016/j.jeem.2023.102846>.

(21) Houston Radar LLC. *Armadillo Tracker Radar Traffic Classifier; Specification Sheet*; Rev 3.1; 2023. https://houston-radar.com/wp-admin/admin-ajax.php?juwpfisadmin=false&action=wpfd&task=file.download&wpfd_category_id=27&wpfd_file_id=3003&token=&preview=1.

(22) Watson, J. G. Overview of Receptor Model Principles. *J. Air Pollut. Control Assoc.* **1984**, *34* (6), 619–623. <https://doi.org/10.1080/00022470.1984.10465780>.

(23) Watson, J. G.; Cooper, J. A.; Huntzicker, J. J. The Effective Variance Weighting for Least Squares Calculations Applied to the Mass Balance Receptor Model. *Atmospheric Environ.* **1967 1984**, *18* (7), 1347–1355. [https://doi.org/10.1016/0004-6981\(84\)90043-X](https://doi.org/10.1016/0004-6981(84)90043-X).

(24) Sug Park, E.; Spiegelman, C. H.; Henry, R. C. Bilinear Estimation of Pollution Source Profiles and Amounts by Using Multivariate Receptor Models. *Environmetrics* **2002**, *13* (7), 775–798. <https://doi.org/10.1002/env.557>.

(25) Paatero, P. Least Squares Formulation of Robust Non-Negative Factor Analysis. *Chemom. Intell. Lab. Syst.* **1997**, *37* (1), 23–35. [https://doi.org/10.1016/S0169-7439\(96\)00044-5](https://doi.org/10.1016/S0169-7439(96)00044-5).

(26) Kumar, A.; Sindhwan, V.; Kambadur, P. Fast Conical Hull Algorithms for Near-Separable Non-Negative Matrix Factorization. In *Proceedings of the 30th International Conference on Machine Learning*; PMLR, 2013; pp 231–239.

(27) Smith, D.; Cyterski, M.; Johnston, J. M.; Wolfe, K.; Parmar, R. ESAT: Environmental Source Apportionment Toolkit Python Package. *J. Open Source Softw.* **2024**, *9* (104), 7316. <https://doi.org/10.21105/joss.07316>.

(28) Dickerson, R. R.; Stratton, P.; Ren, X.; Kelley, P.; Heaney, C. D.; Deanes, L.; Aubourg, M.; Spicer, K.; Dreessen, J.; Auvin, R.; Sawtell, G.; Thomas, M.; Campbell, S.; Sanchez, C. Mobile Laboratory Measurements of Air Pollutants in Baltimore, MD Elucidate Issues of Environmental Justice. *J. Air Waste Manag. Assoc.* **1995** *2024*, *74* (11), 753–770. <https://doi.org/10.1080/10962247.2024.2393178>.

(29) Stull, R. B. *Practical Meteorology : An Algebra-Based Survey of Atmospheric Science*; Department of Earth, Ocean & Atmospheric Sciences, University of British Columbia, 2015. <https://doi.org/10.14288/1.0300441>.

(30) Alessandrini, E. R.; Stafoggia, M.; Faustini, A.; Berti, G.; Canova, C.; De Togni, A.; Di Biagio, K.; Gherardi, B.; Giannini, S.; Lauriola, P.; Pandolfi, P.; Randi, G.; Ranzi, A.; Simonato, L.; Zauli Sajani, S.; Cadum, E.; Forastiere, F.; EpiAir2 Study Group. Association between Short-Term Exposure to PM2.5 and PM10 and Mortality in Susceptible Subgroups: A Multisite Case-Crossover Analysis of Individual Effect Modifiers. *Am. J. Epidemiol.* **2016**, *184* (10), 744–754. <https://doi.org/10.1093/aje/kww078>.

(31) Orellano, P.; Reynoso, J.; Quaranta, N.; Bardach, A.; Ciapponi, A. Short-Term Exposure to Particulate Matter (PM10 and PM2.5), Nitrogen Dioxide (NO2), and Ozone (O3) and All-Cause and Cause-Specific Mortality: Systematic Review and Meta-Analysis. *Environ. Int.* **2020**, *142*, 105876. <https://doi.org/10.1016/j.envint.2020.105876>.

(32) Luben, T. J.; Nichols, J. L.; Dutton, S. J.; Kirrane, E.; Owens, E. O.; Datko-Williams, L.; Madden, M.; Sacks, J. D. A Systematic Review of Cardiovascular Emergency Department Visits, Hospital Admissions and Mortality Associated with Ambient Black Carbon. *Environ. Int.* **2017**, *107*, 154–162. <https://doi.org/10.1016/j.envint.2017.07.005>.

(33) Song, X.; Hu, Y.; Ma, Y.; Jiang, L.; Wang, X.; Shi, A.; Zhao, J.; Liu, Y.; Liu, Y.; Tang, J.; Li, X.; Zhang, X.; Guo, Y.; Wang, S. Is Short-Term and Long-Term Exposure to Black Carbon Associated with Cardiovascular and Respiratory Diseases? A Systematic Review and Meta-Analysis Based on Evidence Reliability. *BMJ Open* **2022**, *12* (5), e049516. <https://doi.org/10.1136/bmjopen-2021-049516>.

(34) Goriaanova, V.; Awada, C.; Opoku, F.; Zelikoff, J. T. Adverse Effects of Black Carbon (BC) Exposure during Pregnancy on Maternal and Fetal Health: A Contemporary Review. *Toxics* **2022**, *10* (12), 779. <https://doi.org/10.3390/toxics10120779>.

**Supporting Information for
Use of multi-pollutant air sensor data and geometric non-negative
matrix factorization for source apportionment of air pollution
burden in Curtis Bay, Baltimore, USA**

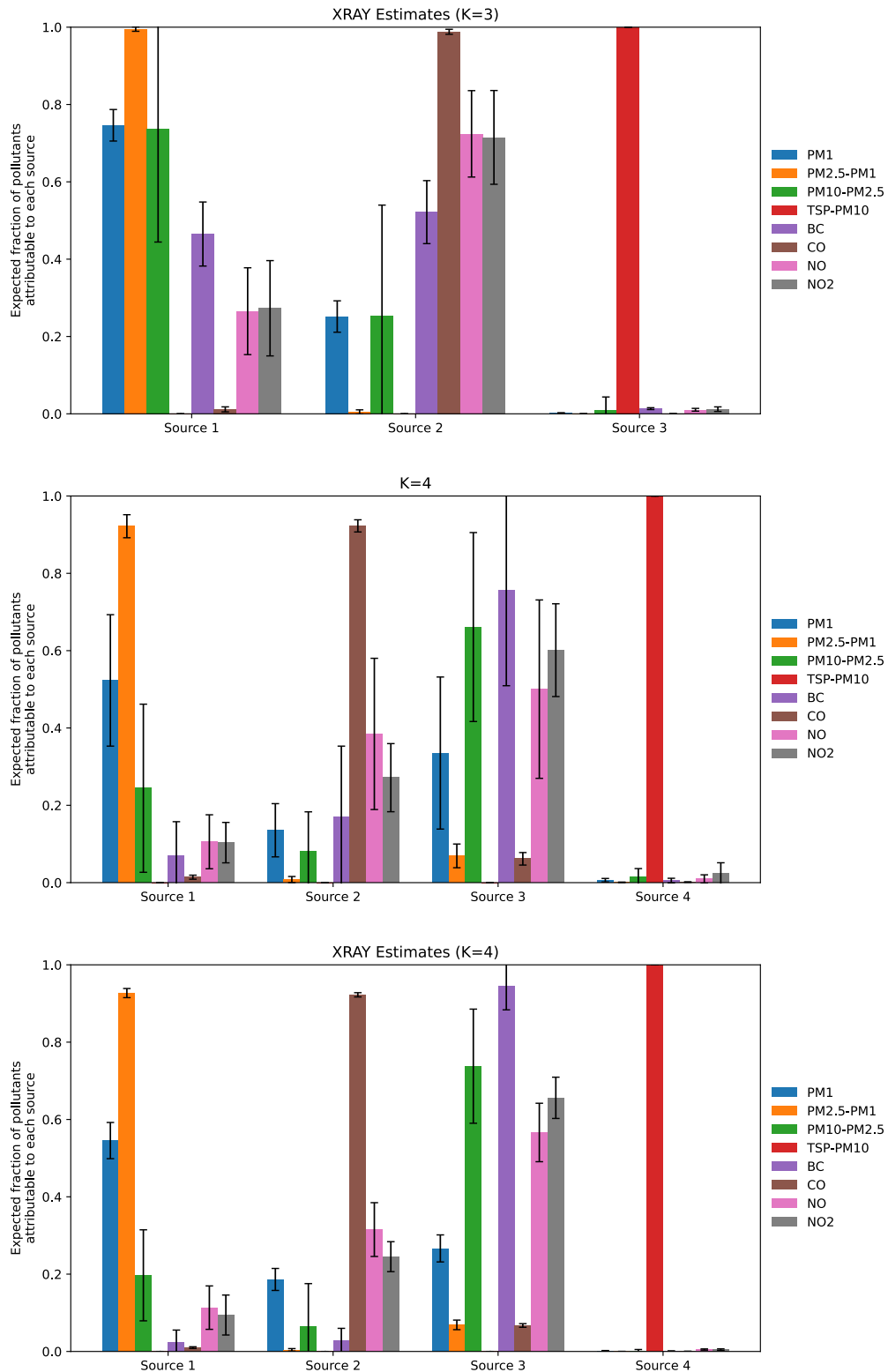
Main results

Table S1. Bootstrap mean (bootstrap SE) of the estimated Φ

	PM₁	PM_{2.5}-PM₁	PM₁₀-PM_{2.5}	TSP-PM₁₀	BC	CO	NO	NO₂
Source 1	0.718 (0.143)	0.985 (0.026)	0.702 (0.310)	0 (<0.001)	0.303 (0.178)	0.024 (0.043)	0.214 (0.134)	0.287 (0.149)
Source 2	0.269 (0.140)	0.014 (0.025)	0.245 (0.282)	0 (<0.001)	0.678 (0.179)	0.974 (0.044)	0.770 (0.136)	0.650 (0.149)
Source 3	0.013 (0.010)	0.001 (0.002)	0.053 (0.130)	1 (<0.001)	0.020 (0.014)	0.002 (0.001)	0.016 (0.018)	0.063 (0.071)

Sensitivity analysis

Figure S1.

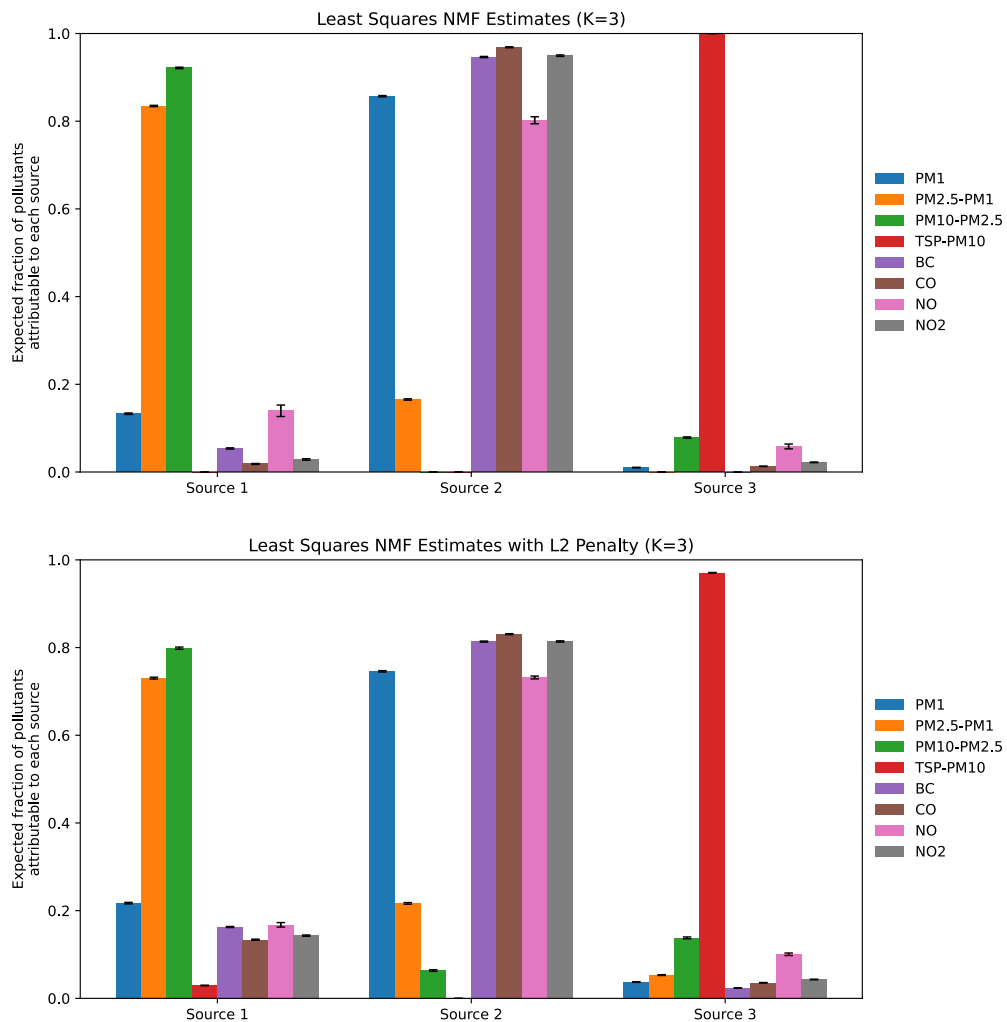


Bootstrap mean \pm standard error (SE) of source attributions estimated by XRAY ($K = 3$; top), the geometric source apportionment method ($K = 4$; middle), and XRAY ($K = 4$; bottom) across 100 resamples. Within a fixed K , the geometric approaches yield highly similar attributions. With $K = 4$, portions of Sources 1 and 2 from the $K = 3$ solution are captured by the additional source.

Table S2. Diagnostics for Φ stability across K . CVar is the mean of cellwise coefficient of variations (bootstrap SE/bootstrap mean); lower values indicate more stable estimates. R is the mean of pollutant-specific rank stability; higher values indicate more consistent identification of the top contributor.

	CVar	R
$K=3$	0.056	0.923
$K=4$	0.050	0.859

Figure S2.

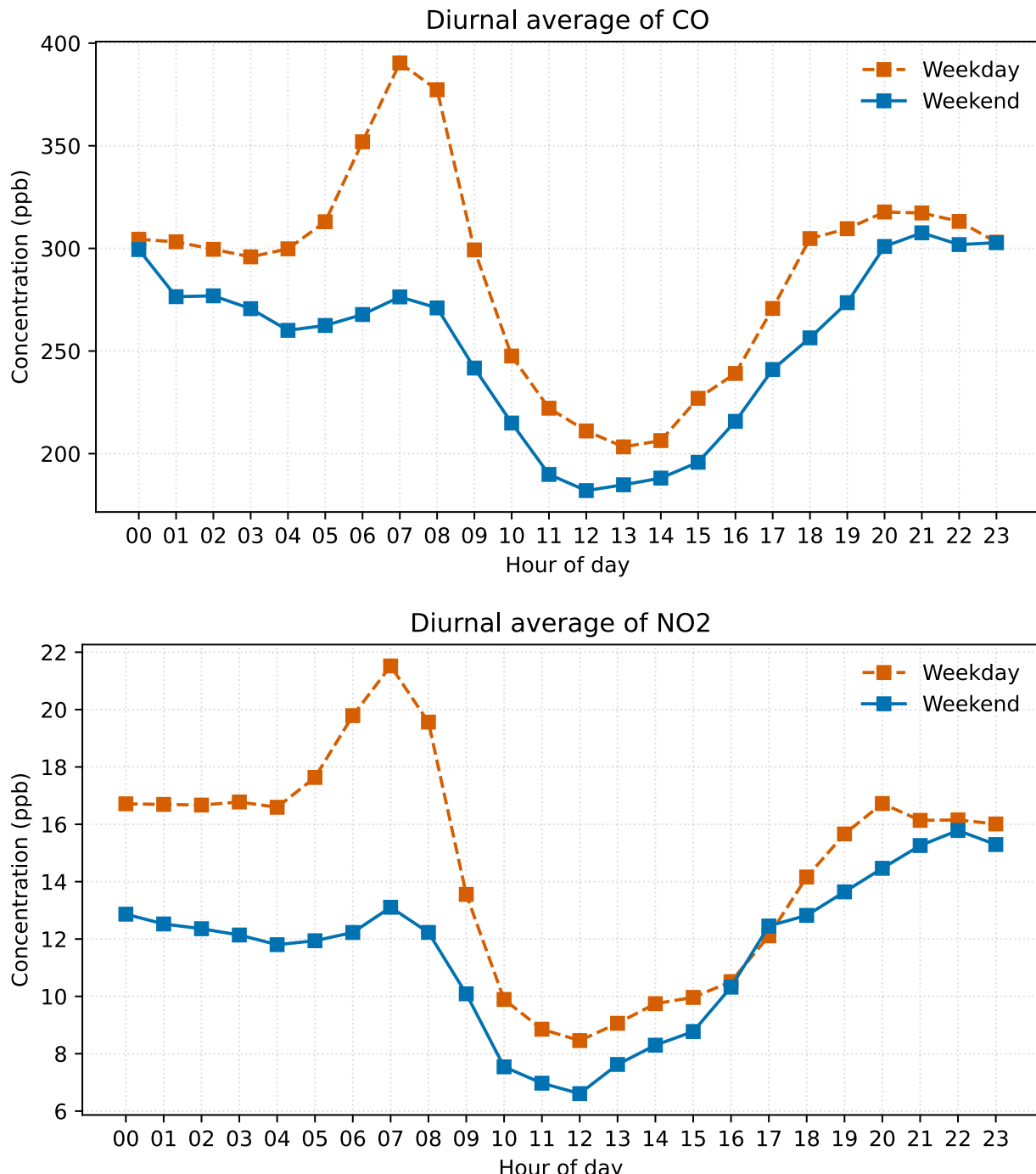


Bootstrap mean \pm SE of source attributions estimated by least squares NMF (obtained using the Python scikit-learn package) with three sources across 100 resamples. Top panel is obtained using the default setting (no regularization), while the bottom panel is obtained using L2 penalization ($\text{alpha_W} = \text{alpha_H} = 0.001$).

On a 2021 MacBook Pro with Apple M1 Pro and 16 GB RAM, using scikit-learn package in Python 3.11, each bootstrap run of the least squares NMF with three sources took 4 seconds on average.

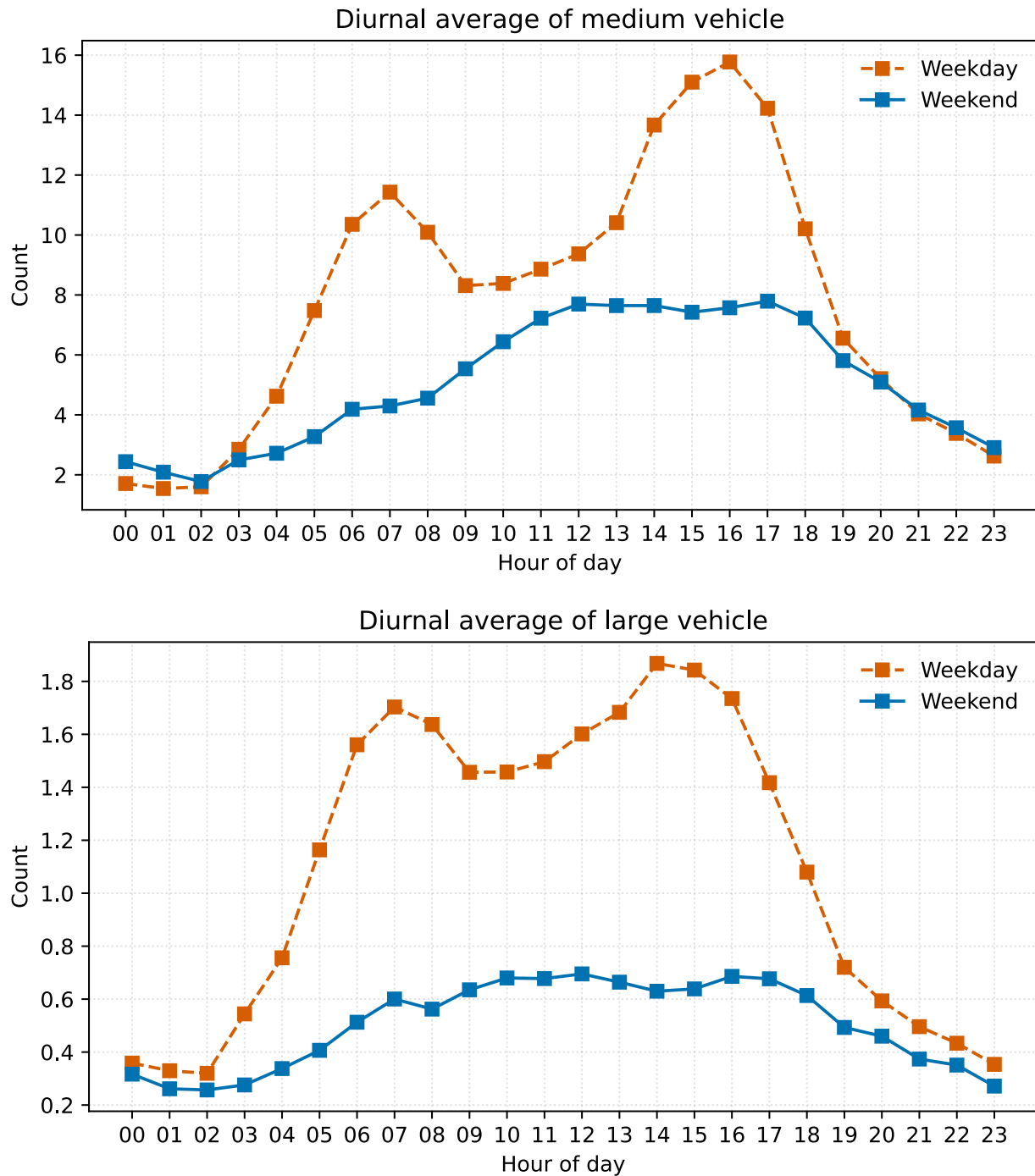
Diurnal patterns

Figure S3.



Diurnal averages of CO (top) and NO₂ (bottom) separately for weekdays and weekends. Source 2 attributes 97% of CO and 65% of NO₂.

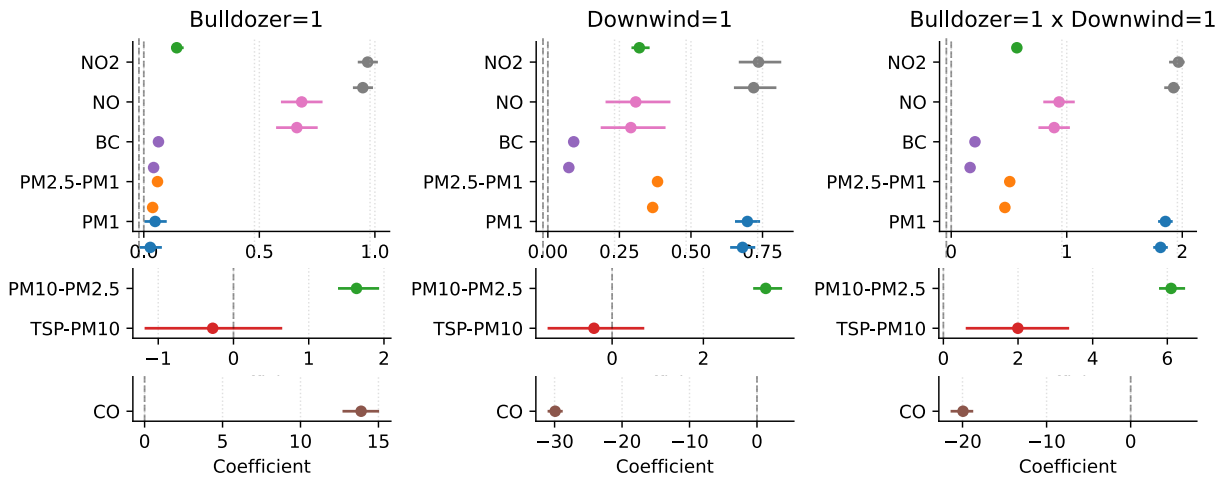
Figure S4.



Diurnal averages of traffic counts by vehicle size, split by weekdays and weekends. “Medium” includes sedans and minivans; “large” includes delivery vans, buses, and dump trucks.

Regression analysis

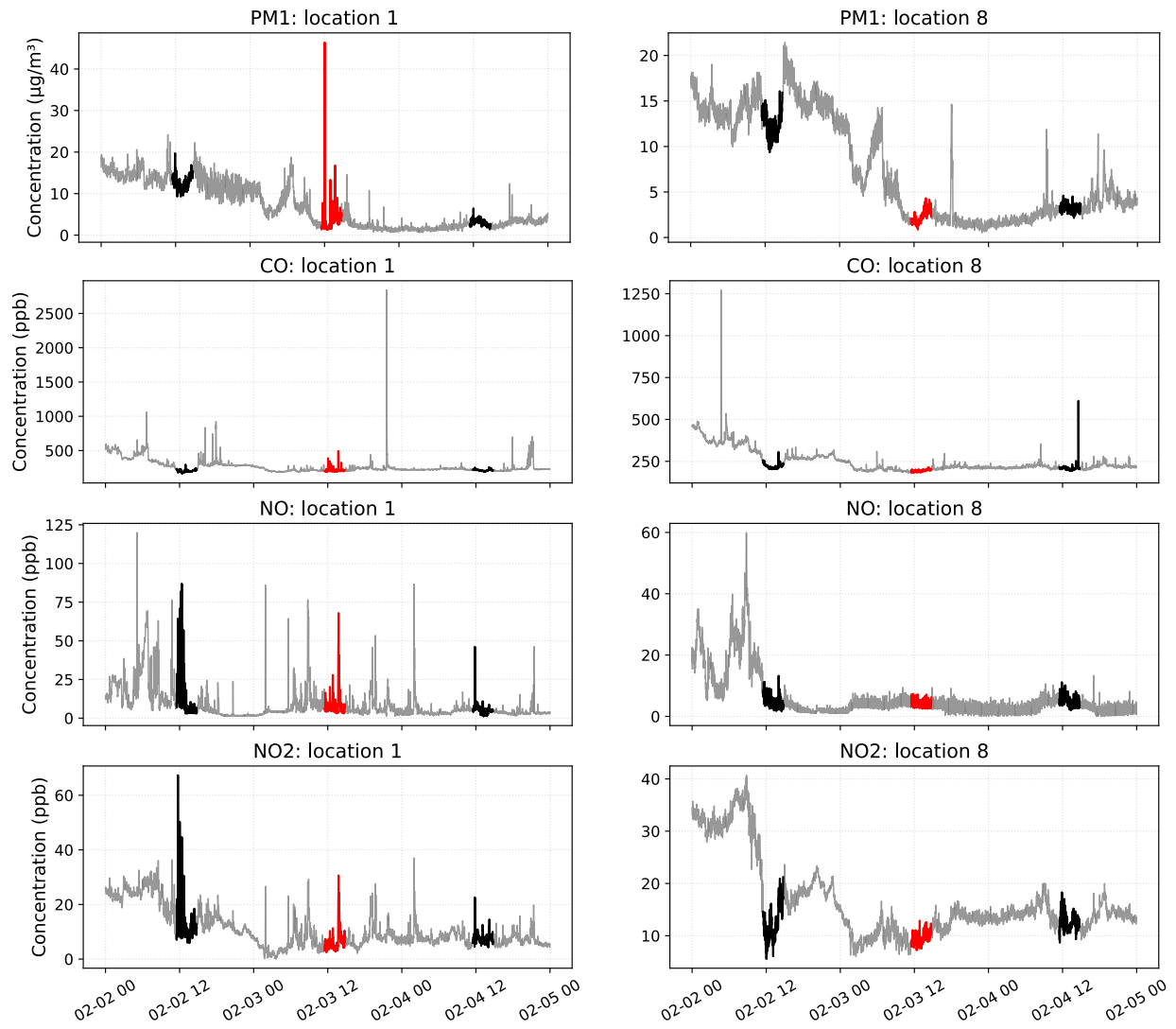
Figure S5.



Linear regressions on individual air pollutants. Points and error bar show bootstrap coefficient means with 95% confidence intervals. Because some coefficients are much larger in magnitude, results for PM₁₀-PM_{2.5}, TSP-PM₁₀, and CO are plotted separately.

Case study

Figure S6.



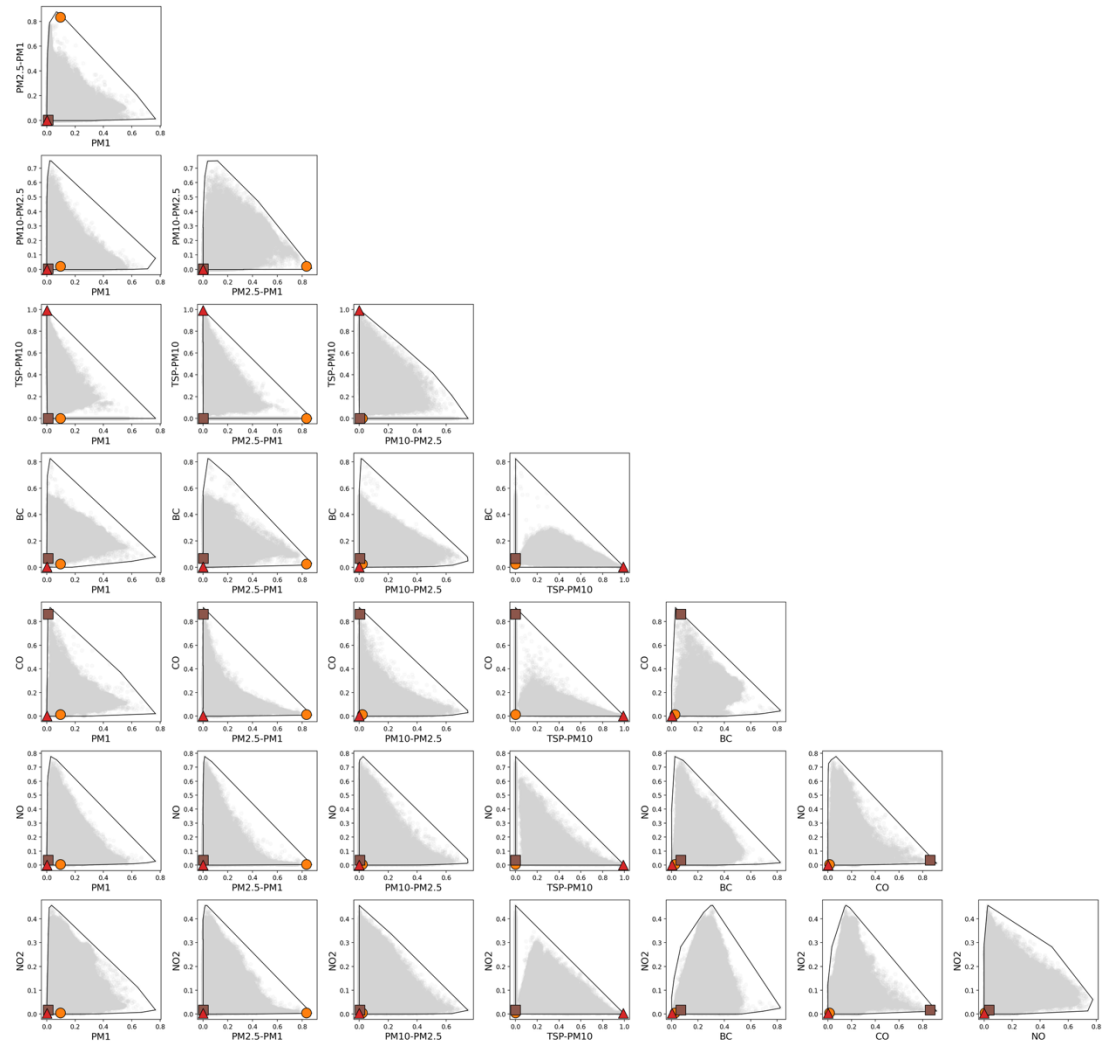
Time series of raw concentrations for the remaining pollutants by location. The incident window (11:30 am – 2:45 pm, February 3, 2023) is highlighted in red; matched comparison hours on the preceding and following days are shown in black. No statistically meaningful distributional differences are observed.

Table S3. Summary statistics for air pollutants of interest from Locations 1 and 8 during the coal-terminal incident versus matched hours on the preceding and following days. We also report p-values from the MW and KS tests.

Pooled	Incident	Count	Mean (Std)	Median	85th percentile	95th percentile	Max	p-value (MW)	p-value (KS)
PM _{2.5} – PM ₁ ($\mu\text{g}/\text{m}^3$)	1	392	2.533 (5.012)	0.782	4.114	10.633	61.349	<0.001	<0.001
	0	784	0.702 (1.205)	0.439	1.035	1.916	17.984		
PM ₁₀ – PM _{2.5} ($\mu\text{g}/\text{m}^3$)	1	392	68.048 (262.682)	22.931	84.842	176.825	3184.519	<0.001	<0.001
	0	784	13.987 (31.422)	4.982	25.488	45.446	451.175		
TSP – PM ₁₀ ($\mu\text{g}/\text{m}^3$)	1	392	70.658 (532.121)	0	42.990	145.961	7392.264	<0.001	<0.001
	0	784	9.659 (126.803)	0	0	36.426	3509.289		
BC ($\mu\text{g}/\text{m}^3$)	1	392	0.472 (0.708)	0.352	1.097	1.819	3.562	1	0.170
	0	784	0.521 (0.458)	0.487	0.950	1.336	2.683		

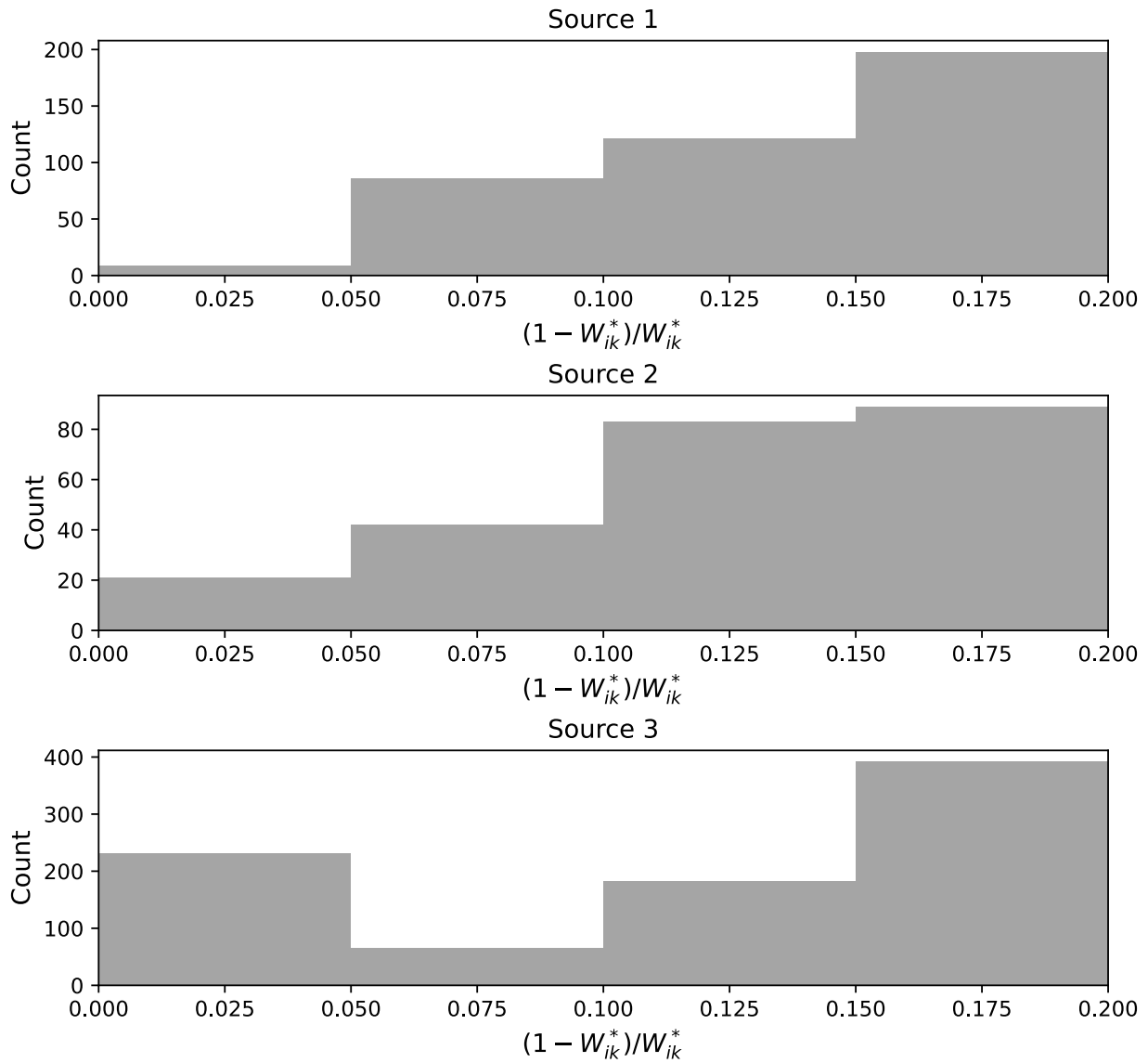
Model adequacy checks

Figure S7.



Boundary of sample convex hull (black lines) of the row-stochastic standardized pollutant concentrations, together with the estimated source profile (orange circle, brown square, and red triangle) whose rows sum to one.

Figure S8.



Assessing probabilistic separability: the ratio $(1 - W_{ik}^*)/W_{ik}^*$ should place nontrivial mass near 0. While it may diverge to infinity, here we restrict attention to $[0, 0.2]$. The matrix W^* is row-normalized version of W .